The Astrophysical Journal Supplement Series, 247:68 (13pp), 2020 April https://doi.org/10.3847/1538-4365/ab72f8

Probing the Galactic Halo with RR Lyrae Stars. I. The Catalog

G.-C. Liu[1], Y. Huang[2,9], H.-W. Zhang[3,4], M.-S. Xiang[5], J.-J. Ren[6], B.-Q. Chen[2], H.-B. Yuan[7], C. Wang[3], Y. Yang[2], Z.-J. Tian[8], F. Wang[3,4], and X.-W. Liu[2,9]

[1] Center for Astronomy and Space Sciences, China Three Gorges University, Yichang 443002, People's Republic of China
[2] South-Western Institute For Astronomy Research, Yunnan University, Kunming 650500, People's Republic of China; yanghuang@ynu.edu.cn, x.liu@ynu.edu.cn
[3] Department of Astronomy, Peking University, Beijing 100871, People's Republic of China
[4] Kavli Institute for Astronomy and Astrophysics, Peking University, Beijing 100871, People's Republic of China
[5] Max-Planck Institute for Astronomy, Königstuhl, D-69117, Heidelberg, Germany
[6] National Astronomical Observatories, Chinese Academy of Science, Beijing 100012, People's Republic of China
[7] Department of Astronomy, Beijing Normal University, Beijing 100875, People's Republic of China
[8] Department of Astronomy, Yunnan University, Kunming 650500, People's Republic of China
Received 2019 August 28; revised 2020 January 31; accepted 2020 February 3; published 2020 April 7

Abstract

We present a catalog of 5290 RR Lyrae stars (RRLs) with metallicities estimated from spectra of the LAMOST Experiment for Galactic Understanding and Exploration (LEGUE) and the Sloan Extension for Galactic Understanding and Exploration (SEGUE) surveys. Nearly 70% of them (3642 objects) also have systemic radial velocities measured. Given the pulsating nature of RRLs, metallicity estimates are based on spectra of individual exposures that have been matched with their synthetic templates. The systemic radial velocities are measured by fitting the observed velocity as a function of phase assuming an empirical pulsating velocity template curve. Various tests show that our analyses yield metallicities with a typical precision of 0.20 dex and systemic radial velocities with uncertainties ranging from 5 to 21 km s^{-1} (depending on the number of radial-velocity measurements available for a given star). Based on the well-calibrated near-infrared $PM_{W1}Z$ or $PM_{K_s}Z$, and M_V–[Fe/H] relations, precise distances are derived for these RRLs. Finally, we include *Gaia* DR2 proper motions in our catalog. The catalog should be very useful for various Galactic studies, especially of the Galactic halo.

Unified Astronomy Thesaurus concepts: RR Lyrae variable stars (1410); Galaxy abundances (574); Chemical abundances (224); Galaxy structure (622); Milky Way stellar halo (1060)

1. Introduction

Probing the Galactic structure is important for understanding the assemblage history of the Milky Way as well as galaxies in general. The Milky Way halo contains some of the oldest stars and structures found in our Galaxy, and thus provides information of the earliest stage of the evolution of our Galaxy. Despite its crucial importance, our knowledge of the stellar halo is still far from complete, partly due to the lack of large samples of halo tracers to probe its properties.

Previously, the main halo tracers employed included blue horizontal branch (BHB) stars (e.g., Xue et al. 2008; Deason et al. 2011, 2014; Das et al. 2016), K giants (e.g., Xue et al. 2015; Xu et al. 2018), near-main-sequence turnoff stars (nMSTO) (e.g., Sesar et al. 2011; Pila-Diez et al. 2015) and RR Lyrae stars (RRLs; e.g., Watkins et al. 2009). The available number of BHB stars is small since they are difficult to identify; distance estimation of K giants is not easy considering that their intrinsic luminosities vary by two orders of magnitude (depending on stellar age and metallicity); and the luminosities of nMSTO are not high enough to be useful for probing the distant outer halo of the Galaxy.

Compared to the other tracers, RRLs are ideal for studying halo properties. First, RRLs are old (>9 Gyr), low-mass metal-poor stars that reside in the instability strip of the horizontal branch (HB) and thus represent a fair sample of the halo populations (Smith 2004). Second, their well defined period–luminosity relation makes them good standard candles, allowing one to accurately map out the 3D structure of the halo. Third, they retain a record of the chemical composition of the environment in which they were born, thus can be used to study the early stage chemical evolution of the Galaxy formation. Finally, they are relatively easy to identify based on their colors and variabilities, enabling the construction of samples of few contaminations. In short, RRLs are excellent tracers to study the structure, formation, and evolution of the Galactic halo.

Nevertheless, time-domain photometric surveys alone cannot provide precise measurements of metallicity and systemic radial velocity of RRLs. Such information has to be extracted from spectroscopic observations. Fortunately, a number of large-scale spectroscopic surveys have been carried out in the past two decades, including the RAVE (Steinmetz et al. 2006), the SDSS/SEGUE (Yanny et al. 2009), the SDSS/APOGEE (Majewski et al. 2017), the LAMOST (Deng et al. 2012; Liu et al. 2014), and the GALAH (De Silva et al. 2015) surveys.

The spectroscopic data, combined with information (e.g., period, phase, and amplitude) derived from light curves provided by photometric surveys and astrometric information (e.g., parallax and proper motions) from *Gaia* DR2, allow one to construct a large sample of RRLs with full phase space information of three-dimensional position and velocity, as well as of metallicity, and to use the sample to probe the formation and evolution of the Galactic halo.

Values of metallicity and radial velocity of RRLs cannot be measured by treating them as normal, steady stars, as RRLs are pulsating and their spectra vary with time on short timescales. To measure the metallicities of RRLs, the most precise method is to utilize high-resolution spectra. High-resolution spectroscopy, however, is quite costly of big telescope time, and no more than a hundred bright local RRLs have been observed this way (e.g., For et al. 2011; Kinman et al. 2012; Nemec et al. 2013;

[9] Corresponding authors.

Table 1
Recent Large-scale Photometric Surveys of RRLs

Survey	Filters	Area (deg^2)	Range of V Magnitude	The Typical Number of Photometric Observations	Observation Year	Sources	Prior	Reference
Catalina	V	~33,000	12–20	60 ~ 419	2004–2011	23,306	5	1
QUEST	*UBVRI*	380/476	13.5–19.7	15 ~ 40	1998–2008	1857	2	2
NSVS	ROTSE-NT	~31,000	$V < 14$	100 ~ 500	1999–2000	1304	0	3
LINEAR	no spectra filter	8000	14–17	200 ~ 460	1998–2009	5684	4	4
LONEOS	LONEOS-NT	1430	$V < 18$	28 ~ 50	1998–2000	838	0	5
SDSS Str82	*ugriz*	249	15–21	30 ~ 40	1998–2006	601	3	6
GCVS	…	…	…	…	…	7954	1	7

Note. The references are: (1) Drake et al. (2013a, 2014), (2) Vivas et al. (2004), Mateu et al. (2012), Zinn et al. (2014), (3) Kinemuchi et al. (2006), Hoffman et al. (2009), (4) Sesar et al. (2013), (5) Miceli et al. (2008), (6) Watkins et al. (2009), Sesar et al. (2010), Süveges et al. (2012), (7) Samus et al. (2009).

Govea et al. 2014; Pancino et al. 2015). For low-resolution spectra, the traditional method to measure the metallicities of RRLs is the so-called ΔS method, first proposed by Preston (1959). The ΔS index describes the difference between the spectral types as given by the H I Balmer lines and by the Ca II K line measured with low-resolution spectra obtained at minimum light. Many studies have been carried out with this method to derive metallicities of RRLs, by calibrating the ΔS relation with either spectroscopic or photometric observations (e.g., Butler 1975; Freeman & Rodgers 1975; Layden 1994). Although this method is efficient, the scale relation between ΔS and [Fe/H] shows some nonlinear variations in some cases, leading to some random and systemic errors in the final results.

In this paper, we present a new method to measure the metallicities of RRLs. For modern large-scale spectroscopic surveys (e.g., the LAMOST and SDSS surveys), there are often two to three exposures made per visit, yielding two to three spectra on a short time span. In addition to the multiple spectra from a single visit, some fields are visited more than once. Excluding spectra affected by shock waves, the metallicity can be measured from the individual single-exposure spectra with a template-matching technique (see Section 3.1 for detail). The mean value, weighted by the signal-to-noise ratios (S/Ns) of estimates yielded by the individual single-exposure spectra, is then adopted as the final metallicity of the RRL.

In addition to metallicity, it is also crucial to precisely measure the systemic radial velocities of RRLs since they are of vital importance for a variety of Galactic studies, such as identifying halo substructures and exploring their origins by kinematics (e.g., Vivas et al. 2001; Keller et al. 2008; Miceli et al. 2008; Casetti-Dinescu et al. 2009; Watkins et al. 2009; Carlin et al. 2012), and constraining the mass distribution of the Milky Way (e.g., Xue et al. 2008; Huang et al. 2016).

However, accurately measuring systemic velocities of RRLs is quite challenging since the observed radial velocities contain a pulsation component of a typical amplitude of several tens of $km\,s^{-1}$ that needs to be accounted for. To derive the values of systemic velocity (RV), two approaches are generally adopted. In one approach, one schedules the observations at the right phase (i.e., $\sim 0.5 \pm 0.1$) such that the pulsation has nearly zero contribution to the observed radial velocity, i.e., $RV_\gamma = RV_{obs}$. This approach, however, is not suitable for data collected with large- scale, multi-object spectroscopic surveys as in our case. Alternatively, one can correct the measured radial velocities for contribution of pulsation assuming a pulsation model (or an empirical template), that describes the pulsation velocity as a function of phase. In this paper, we utilize the latter approach to measure the systemic velocities of RRLs by adopting the empirical template of radial-velocity curves of *ab*-type RRLs as constructed by Sesar (2012).

This paper is the first in a series that utilize RRLs to explore the formation and evolution of the Galactic halo. The data used in the current work are described in Section 2. Estimation of metallicities of RRLs from the spectra is introduced in Section 3. Determinations of systemic radial velocities and distances are presented in Sections 4 and 5, respectively. In Section 6, we present the final catalog and describe its general properties. A summary is given in Section 7.

2. Data

In this section, we first collect known RRLs identified in the various time-domain photometric surveys or variable source catalogs. Then available spectra are searched for those stars in the various large-scale spectroscopic surveys.

2.1. RR Lyrae Stars from Photometric Surveys

To collect known RRLs, we use the catalogs of variable stars from the Quasar Equatorial Survey Team (QUEST; Vivas et al. 2004; Mateu et al. 2012; Zinn et al. 2014), Northern Sky Variability Survey (NSVS; Kinemuchi et al. 2006; Hoffman et al. 2009), Lowell Observatory Near-Earth-Object Search (LONEOS; Miceli et al. 2008), General Catalogue of Variable Stars (GCVS; Samus et al. 2009), the Lincoln Near-Earth Asteroid Research (LINEAR; Sesar et al. 2013) and the Catalina (Drake et al. 2013a, 2014) surveys. Data of the southern hemisphere are not included since only spectroscopic data in the northern sky are used (see next Section). A prior is set to each survey (see Table 1), according to their observational epochs (higher prior for those surveys more close to the spectroscopic observations described as follows) and the typical number of photometric observations. For each survey, we compile all the available parameters of identified RRLs into a single catalog, including period, amplitude, epoch, mean V-band magnitude, variable star type, and distance if derived. In total, we obtain a list of 32,243 unique RRLs from those surveys.

Table 1 summarizes the properties of the individual surveys included in the current study. Figure 1 plots the distributions of the stars in Galactic coordinates, in distances (adopted directly from the literature), in mean V-band magnitudes, and in periods. If a parameter of a given star is available from more than one survey, then the value from the survey with highest prior is adopted.

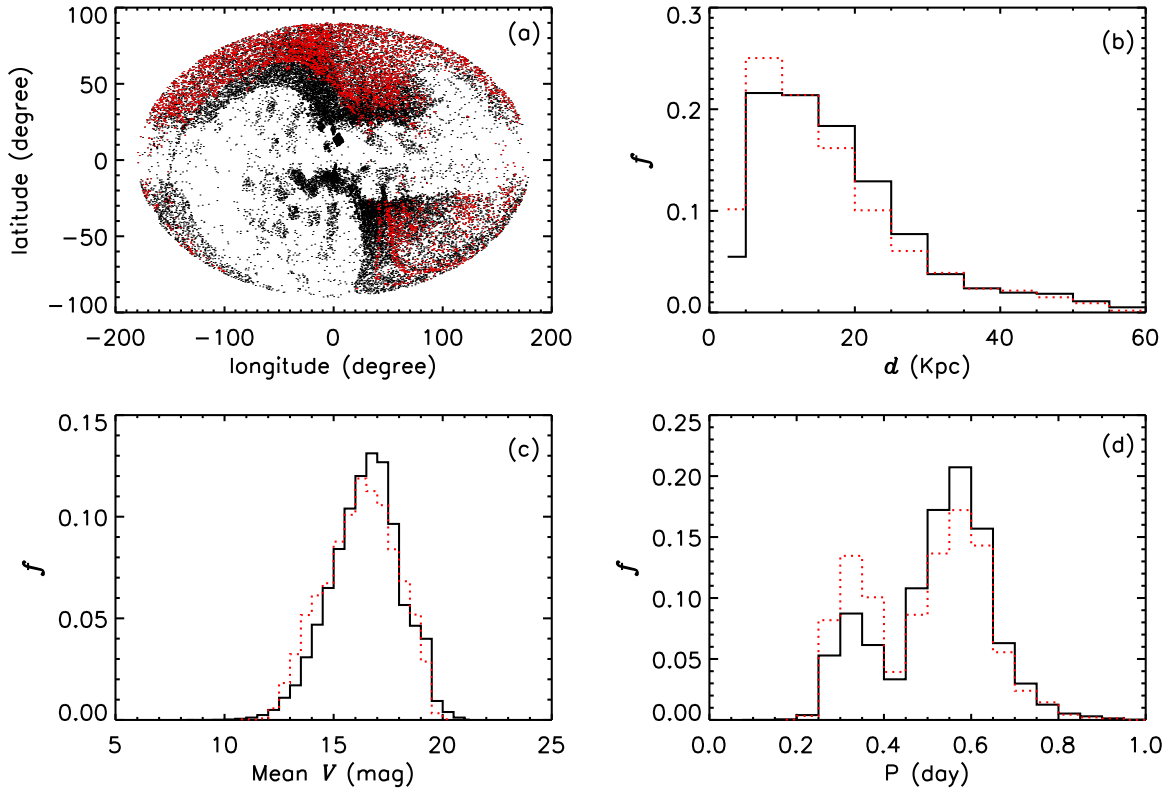

Figure 1. Basic properties of our photometric (black dots/lines) and spectroscopic (red dots/lines) RRL samples. Panel (a) shows the spatial distribution in Galactic coordinates. Panel (b) shows the normalized distribution of distances collected from the literature. Panel (c) shows the normalized distribution of mean *V*-band magnitudes. Panel (d) shows the normalized distribution of periods.

Finally, we note that the catalogs of Drake et al. (2013b, 2014) do not provide the epochs of maximum light for the cataloged RRLs. For those stars, we have calculated the missing values by ourselves from the light curves provided by the Catalina survey.[10]

2.2. Spectroscopy

In the current work, our major spectroscopic data set comes from the LAMOST Galactic spectroscopic surveys (Deng et al. 2012; Zhao et al. 2012; Liu et al. 2014). LAMOST (also named Guoshoujing Telescope) is an innovative quasi-meridian reflecting Schmidt telescope capable of simultaneously recording spectra of up to 4000 objects in a large field of view (FoV) of 5 degrees in diameter. The spectra cover the wavelength range from 3700 to 9100 Å with a resolving power $R \sim 1800$. Typically, $2 \sim 3$ exposures are obtained for each plate, with typical integration time per systemic velocity exposure of 10–40 minutes, depending on the brightness of targeted sources. Since the LAMOST FoV is circular, field overlapping cannot be avoided in order to achieve a contiguous sky coverage. About 25% of all targets have been observed twice and over 2% have been three times (Yuan et al. 2015). This greatly benefits the measurements of systemic radial velocity of RRLs reported in this work. By 2016 June, the LAMOST Galactic surveys, initiated in 2012 October, have obtained ~6 million quality spectra, mostly of Galactic stars. This number is still increasing at a rate of 1 million per annum.

Another main source of spectra comes from the Sloan Digital Sky Surey (SDSS)/Sloan Extension for Galactic Understanding and Exploration (SEGUE; Yanny et al. 2009). As a major component of the SDSS-II, SEGUE operated from 2005 August to 2008 July, and obtained more than 240,000 spectra of Galactic stars of magnitudes $14.0 < g < 20.3$, with a spectral coverage and resolution similar to those of LAMOST. In order to obtain spectra of sufficient S/Ns, the typical total integration time for bright plates of sources of ($14.0 < r < 17.8$) is 1 hr and that for plates of fainter sources of $17.8 < r < 20.1$ is 2 hr. The integration time of the individual exposures ranges between 10 and 30 minutes. SEGUE-2, the successor of SEGUE, obtained an additional 155,520 spectra with the same instrument. All the data from SEGUE and SEGUE-II are included in SDSS Data Release 12 (SDSS DR12; Alam et al. 2015).

The spectral database of SDSS DR12 is downloaded and then cross-matched with the aforementioned compiled catalog of photometrically identified RRLs. In total, 3834 common stars are found, with a total of 20,772 single-exposure spectra. Similarly, a total of 3016 common sources (with a total of 10,667 single-exposure spectra) are found between the photometric catalog of RRLs and the LAMOST DR2 value-added catalog (Xiang et al. 2015, 2017). By combining the two data sets, a total of 6268 RRLs with a total of 31,439 single-exposure spectra are obtained. Typical S/Ns of those single-exposure spectra are around 15.

3. Spectroscopic Metallicities

As mentioned above, we utilize single-exposure spectra instead of those combined to measure the metallicities, given the pulsating nature of RRLs.

3.1. Measurement Method

To estimate the metallicities of RRLs from single-exposure spectra, we adopt a template-matching method by comparing

[10] http://nesssi.cacr.caltech.edu/DataRelease/RRL.html

the observed spectra with the synthetic ones based on the least-χ^2 technique. The synthetic spectra library was generated with version 2.76 of the code SPECTRUM (Gray 1999), utilizing the Kurucz stellar model atmospheres of Castelli & Kurucz (2003) that cover the wavelength range from 3850 to 5600 Å at a resolution of 2.5 Å. We degrade the model spectral resolution to match that of LAMOST and SDSS ($R \sim 1800$). Considering the typical ranges of atmospheric parameters of RRLs, we limit our synthetic spectra to parameter ranges: effective temperature $6000 \leqslant T_{\rm eff} \leqslant 7500$ K in steps of 100 K, surface gravity $1.5 \leqslant \log g \leqslant 4.0$ dex in steps of 0.25 dex, and metallicity $-3.0 \leqslant$ [Fe/H] $\leqslant 0.0$ dex in steps of 0.1 dex. Considering the old (typically >9 Gyr) and metal-poor nature of RRLs, we fix the value of the α-element to iron abundance ratio [α/Fe] to 0.4.

In order to more precisely obtain the parameters $T_{\rm eff}$ and [Fe/H], we match the observed spectra with the synthetic ones by two steps. First, we measure the effective temperature $T_{\rm eff}$ by least-χ^2 fitting. Considering that the Balmer lines are most sensitive to effective temperature, we give two times the weights (weighted by the inverse variances of the spectral fluxes) of the spectral pixels that cover for Hα, Hβ, and Hγ lines when comparing the full observed spectra with the synthetic ones in the wavelength range 3850 to 5600 Å pixel by pixel. At this step, effective temperatures are well determined from single exposure spectra.[11] The derived effective temperatures are then set as input values at the following second round of fitting. In the second step, values of the Ca II K line (mostly sensitive to metallicity) and the continuum with the synthetic one but fixing $T_{\rm eff}$ to the value are deduced from the first step. In this step, spectral pixels covering Ca II H and the Balmer lines, i.e., pixels of the wavelength ranges 3960–3980, 4092–4112, 4330–4350, and 4851–4925Å, are masked out. Best-fit values of [Fe/H] and $\log g$ yielding this second round of optimization are adopted for the star. Figure 2 plots the resulting stellar atmospheric parameters of an RRL as a function of phase. For this particular target, a total of 12 single-exposure spectra are available. We find that the estimated values of $T_{\rm eff}$ and $\log g$ vary with the phase of pulsation, largely consistent with theoretical predictions.

In the above two steps, the metallicities of RRLs are obtained from the individual single-exposure spectra. In principle, no matter what the pulsation stage of the RRL is when targeted, its metallicity should unchange and keep the same value. However, due to the effects of shock waves on the hydrogen and metal lines of RRL spectra (Fokin 1992; Gillet & Fokin 2004; Pancino et al. 2015), the estimated [Fe/H] could change significantly depending on the phase when the spectrum was taken. As Figure 2 shows, the metallicities of RRLs estimated during phases between 0 and 0.15 vary dramatically, reflecting the significant effects of shock waves during those phases during the pulsation cycle. To avoid the potential bias in the metallicity determinations caused by shock waves, we try to exclude single-exposure spectra possibly affected by the shock effects for parameter estimates. In general, shock waves mostly occur during phases 0–0.15 and 0.85–1.0, but they also can happen at other phases. Considering that the Ca II K line is easily affected by the shock wave effects, here we adopt its equivalent width (EW) as a criteria to assess whether a spectrum is affected by shock waves or not.

[11] Surface gravity and metallicity are also estimated at this step but they are not well constrained due to high weights on Balmer lines and thus have not been used.

We first calculate the values of EW of the Ca II K line, EW(Ca II K), of all model spectra and find the minima for each effective temperature. Then we fit the minima as a function of temperature with a second-order polynomial and find Min[EW (Ca II K)] $= 15.62 - 0.0037\,T_{\rm eff} + 2.21 \times 10^{-7}\,T_{\rm eff}^2$. At the same time, we also calculate the EW(Ca II K) for each of the single-exposure spectra of our sample stars. As Figure 2 shows, we find that the values of metallicity measured from single-exposure spectra of EW(Ca II K) less than the corresponding Min[EW(Ca II K)] are different from those measured at other phases (see Panel (d) of Figure 2). This indicates that the former spectra are affected by shock waves and metallicities yielded by those spectra were consequently ignored. The final adopted metallicity and its error are the weighted mean (by its errors), yielded by single-exposure spectra (see Section 3.2.1), if the number of metallicity measurements is greater than 2. If only a single spectrum is available for a star, we directly use the metallicity of this single spectrum as the final adopted value of this star. Finally, we obtain the metallicities for 5290 RRLs. It should be noted that Fabrizio et al. (2019) also estimated the metallicities of 2382 fundamental RRLs by ΔS method.

By comparing the metallicity estimate of common stars selected from LAMOST and SEGUE s with similar S/Ns (i.e., ΔS/N $\leqslant 5$), a negligible offset (around 0.04 dex) is found between the metallicity measurements from the spectra obtained by the two surveys. We therefore assume the metallicity scales yielded from the two surveys are the same.

3.2. Validation of Metallicities

In this section, we examine the accuracy of metallicities of RRLs measured by the above method in the following ways. (1) Check the internal uncertainties using duplicate observations. (2) Check both the random and systemic errors by comparing with metallicity measurements from high-resolution spectroscopy.

3.2.1. Comparison of Results from Multi-epoch Observations

To estimate the internal errors of the metallicities derived, we use multi-epoch observations of our sample stars. The differences of two metallicity measurements of similar S/Ns (i.e., ΔS/N < 10) as a function of the mean S/N are shown in Figure 3. As the figure shows, the median differences are almost zero, with no significant systemic trend. As expected, the standard deviations of the differences decrease with S/N. We fit the standard deviations (divided by $\sqrt{2}$) as a function of S/N, and find s.d./$\sqrt{2} = 0.08 + 2.04$/S/N. For the observations reported here, the typical standard deviation is about 0.2 dex. We use the standard deviations derived by the above function as the error (σ_i) of the metallicity estimated by an individual single-exposure spectrum when it has an S/N less than 40, and for S/N $\geqslant$40, the errors are fixed to the value of $0.08+2.04/40 = 0.13$ dex.

3.2.2. Comparison of Results with Reference Stars

In order to check the zero-points of our metallicity measurements, we collect reference stars from the literature with reliable metallicity estimates either from high-resolution spectroscopy or as a member star of a globular cluster (GC). For GC member stars, we use a compiled catalog of over 3000 variable stars in 103 GCs (Clement 2017). The properties (e.g., metallicities, radial velocities and distances) of those GCs are

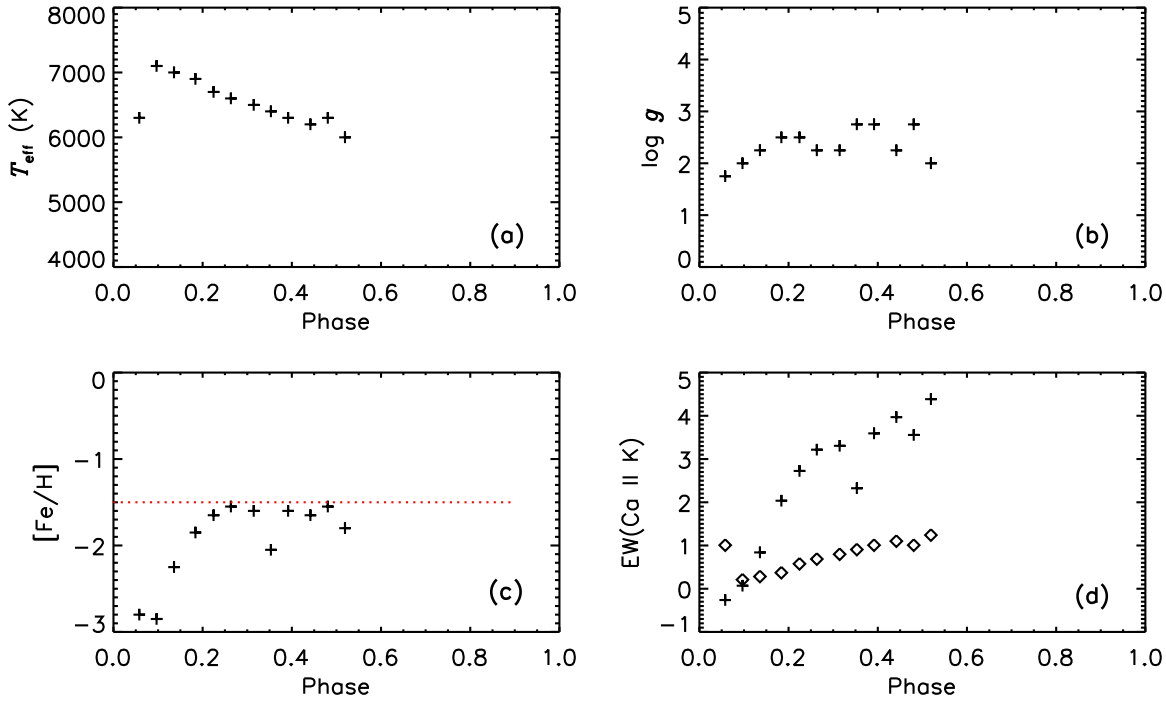

Figure 2. Atmospheric parameters of single-exposure spectra obtained by template-matching for SDSS J134134.54+281855.2 with 12 exposures, which is a member star of globular cluster NGC 5272. Panel (a) shows the effective temperature varies with phase. Panel (b) shows the log g varies with phase. Panel (c) shows the measurement of metallicity at different phases; the dashed line shows the reference metallicity given by Harris (2010). Panel (d) shows the equivalent width of the Ca II K line EW(Ca II K) at different phases. In Panel (d), the plus symbols represent the calculated values of EW(Ca II K) from 12 single-exposure spectra and the diamond symbols indicate the minimal value of EW(Ca II K) of model spectra with the same $T_{\rm eff}$ as that from observed single-exposure spectra (estimated by the first round of fitting; see Section 3.1 for details).

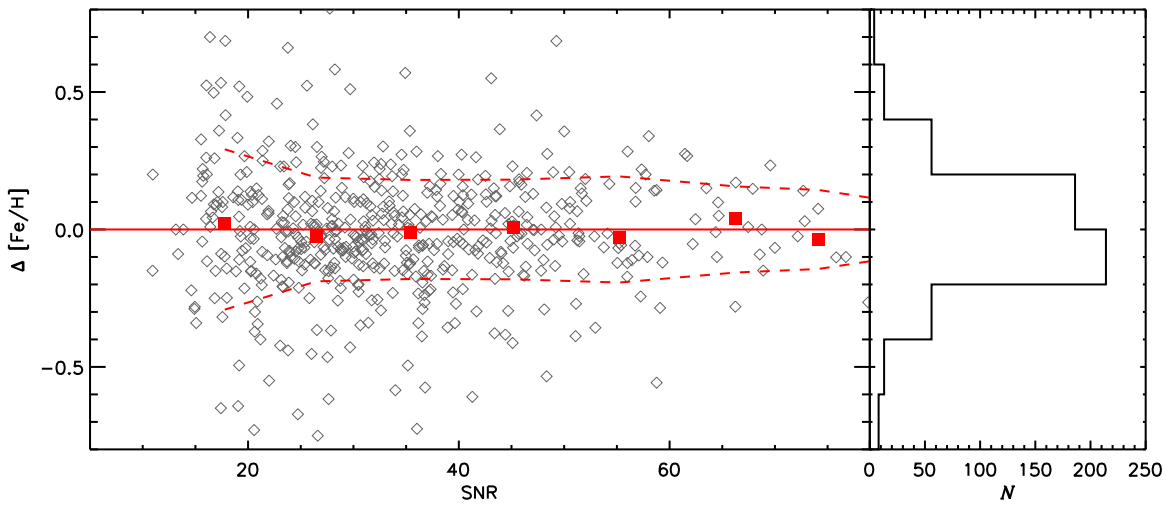

Figure 3. Left panel: difference of metallicities yielded by multi-epoch observations plotted against S/Ns. The red dashed lines mark the standard deviations. The red squares indicate the average of the differences in the individual S/N bins and the red solid line delineates zero differences. Right panel: histogram of the differences.

taken from Harris (2010). The metallicity scale adopted here is the one established by Carretta et al. (2009), which is a fundamental shift from the older metallicity scale (Zinn & West 1984) with superior abundance analysis methods based on more advanced model atmospheres. In addition, we have collected stars with metallicity and systemic radial-velocity estimates measured with high-resolution spectroscopy (e.g., Clementini et al. 1995; For et al. 2011; Kinman et al. 2012; Nemec et al. 2013; Govea et al. 2014; Pancino et al. 2015). We have cross-matched our RRLs spectroscopic sample with the above compiled catalogs and obtained 47 stars in common. Those common stars form our reference star sample. Tables 2 and 3 present relevant information of the reference stars, for GC members and from high-resolution spectroscopy, respectively.

As Figure 4 shows, the values of metallicity estimated in the current work agree well with those of the compiled reference stars, with a negligible offset (−0.04) and a standard deviation of 0.22 dex. The dispersion is comparable to that yielded by multi-epoch observations. All the tests shows that intrinsic consistency of our measurements is good.

In addition, we have also compared the metallicity measurements yielded by the default SEGUE and LAMOST pipelines with the literature values for reference stars. As

Table 2
Parameters of Reference Stars from Globular Clusters

Cluster	R.A. (degree)	Decl. (degree)	[Fe/H]	RV (km s^{-1})	RV$_{err}$ (km s^{-1})	Distance(kpc)	N
NGC 4147	182.544	18.581	−1.80	183.2	0.70	19.3	1
NGC 5053	198.997	17.741	−2.27	44.0	0.40	17.4	2
NGC 5024	198.359	18.162	−2.10	−62.9	0.30	17.9	3
NGC 5272	205.392	28.507	−1.50	−147.6	0.20	10.2	11
NGC 5466	211.373	28.507	−1.98	−106.9	0.20	16.0	2
NGC 5904	229.827	2.283	−1.29	53.2	0.40	7.5	1
NGC 6341	259.300	43.207	−2.31	−120.0	0.10	8.3	1
NGC 7089	323.471	−0.799	−1.65	−5.3	2.0	11.5	2
NGC 7078	322.580	12.316	−2.37	−107.0	0.20	10.4	2
Pal 5	228.991	−0.190	−1.41	−58.7	0.20	23.2	4

Table 3
Metallicity of Reference Stars from High-resolution Spectroscopy

Star	R.A. (degree)	Decl. (degree)	[Fe/H]	[Fe/H]$_{err}$	Reference
DR And	16.295	34.218	−1.37	0.12	Pancino et al. (2015)
BK Eri	42.483	−1.420	−1.72	0.21	Pancino et al. (2015)
SZ Gem	118.431	19.273	−1.65	0.07	Pancino et al. (2015)
SS Leo	173.477	−0.033	−1.48	0.07	Pancino et al. (2015)
UV Vir	185.320	0.368	−1.10	0.12	Pancino et al. (2015)
UZ CVn	187.615	40.509	−2.21	0.13	Pancino et al. (2015)
RV UMa	203.325	53.988	−1.20	0.08	Pancino et al. (2015)
TW Boo	221.275	41.029	−1.47	0.05	Pancino et al. (2015)
VIII-14	256.891	58.850	−2.92	···	Kinman et al. (2012)
V355 Lyr	283.358	43.155	−1.14	0.17	Nemec et al. (2013)
KIC 11125706	285.245	48.745	−1.09	0.08	Nemec et al. (2013)
NQ Lyr	286.952	42.300	−1.89	0.10	Nemec et al. (2013)
NR Lyr	287.114	38.813	−2.54	0.11	Nemec et al. (2013)
FN Lyr	287.593	42.459	−1.98	0.09	Nemec et al. (2013)
V838 Cyg	288.516	48.200	−1.01	0.10	Nemec et al. (2013)
V1104 Cyg	289.502	50.755	−1.23	0.15	Nemec et al. (2013)
V1107 Cyg	289.939	47.1012	−1.29	0.23	Nemec et al. (2013)
V2470 Cyg	289.991	46.889	−0.59	0.13	Nemec et al. (2013)
V894 Cyg	293.254	46.240	−1.66	0.12	Nemec et al. (2013)

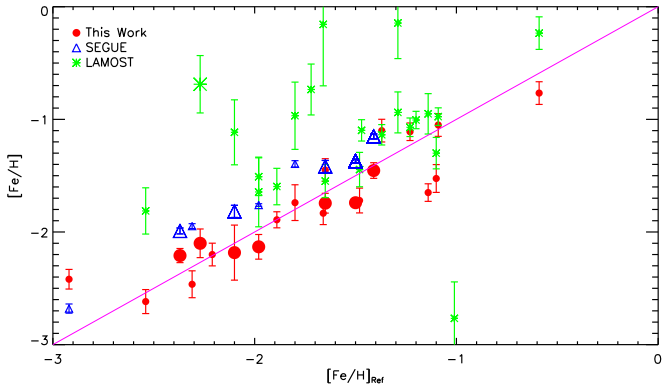

Figure 4. The metallicities of reference stars estimated in the current work (red dots), and those given by the default SEGUE (blue triangles) and LAMOST (green stars) pipelines, are plotted against the literature values. Stars in globular clusters are averaged in a single dot and represented by larger symbols.

Figure 4 shows, both pipelines overestimate the metallicities, significantly.

4. Systemic Radial Velocities

As mentioned in Section 1, it is of crucial importance to measure the systemic radial velocities of RRLs. In this Section, we use the empirical template radial-velocity curves of RRLs to fit the observed radial velocities as a function of phase as derived from the individual single-exposure spectra of RRLs in order to obtain their systemic radial velocities.

4.1. Measurement Method

Here, we adopt the empirical template radial-velocity curves of *ab*-type RRLs constructed by Sesar (2012) for Hα, Hβ, and Hγ lines. According to Figure 3 of Sesar (2012), the uncertainty of systemic velocity yielded by fitting the empirical templates increases dramatically for observational phases greater than 0.7. On the other hand, spectra at phases less than 0.1 are liable to strong effects of shock waves. Consequently, we decide to only use single-exposure spectra taken at phases between 0.1 and 0.7. Among those, spectra affected by shock waves, as implied by the criteria EW(Ca II K) $<$ Min [EW(Ca II K)], are further excluded when deriving the systemic velocity by fitting with the radial-velocity template.

For those with an adopted single-exposure spectrum, we derive the observed RV by fitting Hα, Hβ, and Hγ line profiles with a Gaussian function, together with a first-order polynomial, and measure their centers (wavelength coverage from 4325 to 4357 Å for Hγ lines, 4845 to 4878Å for Hβ lines, and 6548 to 6580 Å for Hα lines, are respectively used in the fits.).

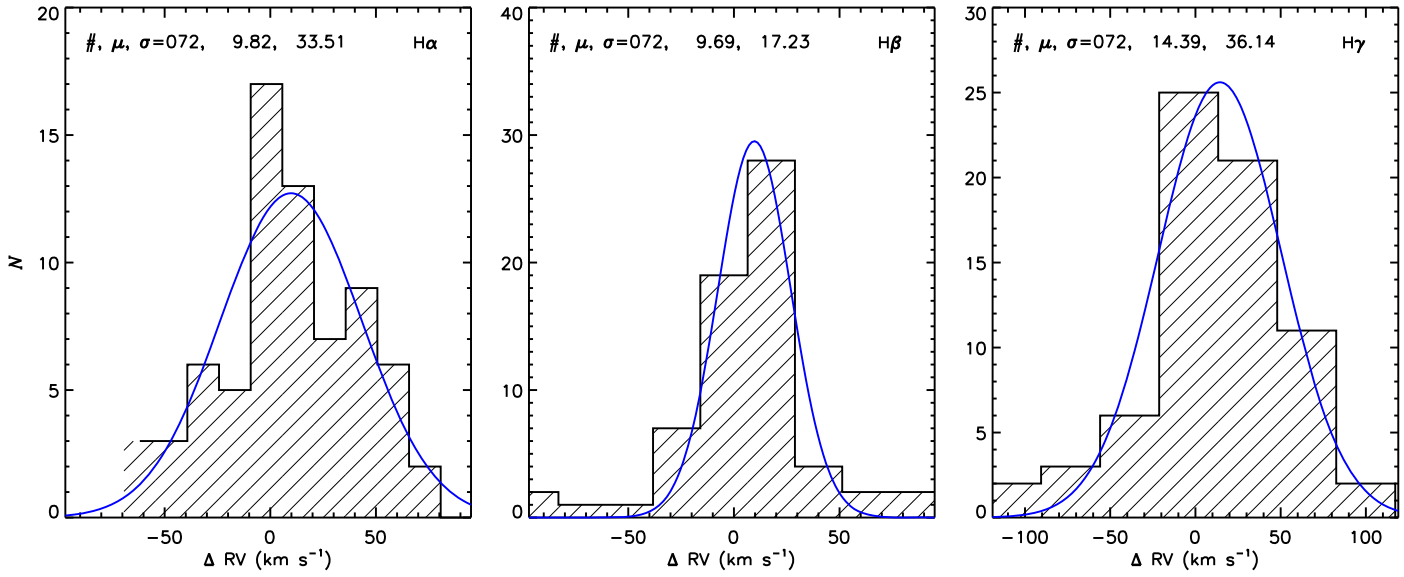

Figure 5. Distributions of values of ($RV_{LAMOST} - RV_{SDSS}$) as measured from Hα (left), Hβ (middle), and from Hγ (right) lines, respectively. The three numbers marked in the top left of each panel denote the number of common stars, the mean and the standard deviation of the RV difference between LAMOST and SDSS, respectively. The blue lines represent the Gaussian fit.

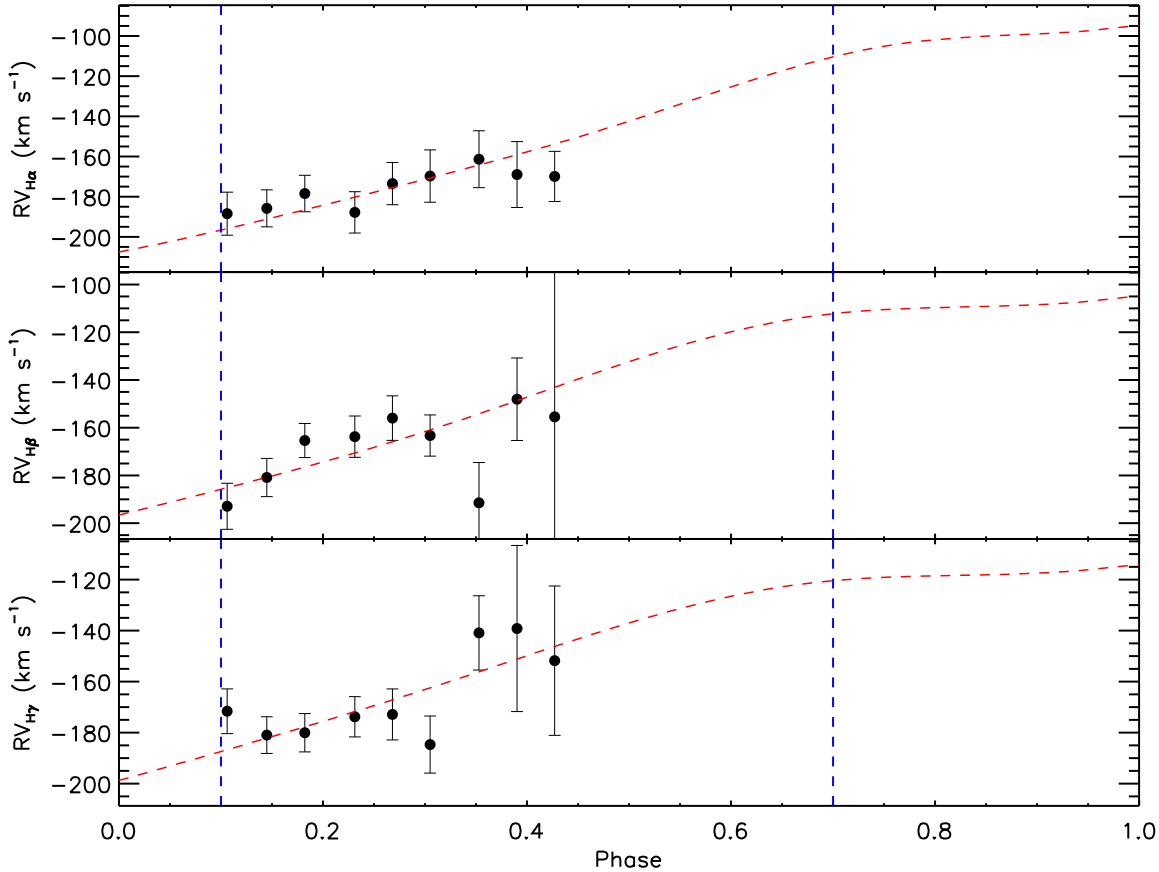

Figure 6. As an example, radial velocities (black dots with error bars) measured from Hα (top panel), Hβ (middle panel), and Hγ (bottom panel) are fitted with the radial-velocity templates constructed by Sesar (2012) (red dashed line), with the blue dashed lines marking the fitting range ($0.1 \leqslant$ phase $\leqslant 0.7$).

Considering that we use spectra from two surveys (LAMOST and SDSS), radial velocities derived from spectra of the two surveys need be calibrated to a common scale. Common sources from the two surveys with similar phases (Δphase < 0.05) and high S/Ns (>50) are selected, yielding a total of 72 targets. Distributions of the RV differences (LAMOST values minus SDSS ones) for different lines (i.e., Hα, Hβ, and Hγ) are shown in Figure 5. The medians and standard deviations estimated from the distributions are, respectively, 9.82 ± 33.51, 9.69 ± 17.23, and 14.39 ± 36.14 km s^{-1}

Table 4
Internal Errors from Three Balmer Lines for Different Numbers for Available Measurements Used in the Fit

n	$\sigma_{H\alpha}$ (km s^{-1})	$\sigma_{H\beta}$ (km s^{-1})	$\sigma_{H\gamma}$ (km s^{-1})
1	25.19	15.81	28.81
2	20.17	8.57	20.46
3	15.25	6.57	13.85
$\geqslant$4	12.05	5.72	10.83

for Hα, Hβ, and Hγ. We then calibrate LAMOST RVs derived from the three lines to the scales of SDSS, using the median differences found above.

For a given star that has RV_{obs} measured at several phases, one can derive the systemic velocity RV by fitting the following equation:

$$RV_{obs}(\Phi_{obs}) = A_{rv}T(\Phi_{obs}) + RV, \quad (1)$$

where Φ_{obs} is the observational phase, A_{rv} the amplitude of the radial-velocity curve, fixed to the mean values reported in Table 1 of Sesar (2012), i.e., 111.9, 90.9, and 82.1 km s^{-1} for Hα, Hβ, and Hγ, respectively, and $T(\Phi_{obs})$ is the radial-velocity curve template. If only one radial-velocity measurement is available, we directly interpolate the template to get the systemic radial-velocity. As an example, Figure 6 shows the fit for a source with nine phase data points.

From the above procedure, the final systemic radial velocity adopted for a given star is given by the weighted mean (by uncertainties) of measurements yielded by the three Balmer lines, i.e., $RV_{H\alpha}$, $RV_{H\beta}$ and $RV_{H\gamma}$. Basically, the measurement uncertainties are highly dependent on the number of radial-velocity measurements used in the fitting.

To derive the random errors of systemic velocity measurements from the individual lines, we solve the following equations:

$$\sigma_\alpha^2(n) + \sigma_\beta^2(n) = \sigma_{\alpha\beta}^2(n), \quad (2)$$

$$\sigma_\alpha^2(n) + \sigma_\gamma^2(n) = \sigma_{\alpha\gamma}^2(n), \quad (3)$$

$$\sigma_\beta^2(n) + \sigma_\gamma^2(n) = \sigma_{\beta\gamma}^2(n). \quad (4)$$

Here n is the number of available radial-velocity measurements for a given star and $\sigma_{\alpha\beta}(n)$, $\sigma_{\alpha\gamma}(n)$, and $\sigma_{\beta\gamma}(n)$ are standard deviations of the differences of systemic velocities measured from two out of three lines for a given n.

Table 4 lists those σ values for different values of n for Hα, Hβ, and Hγ lines. We compare values of $RV_{H\alpha}$ and $RV_{H\beta}$ with those of $RV_{H\gamma}$ and obtain mean values of differences 14.59, and 5.83 km s^{-1} for $RV_{H\alpha} - RV_{H\gamma}$, and $RV_{H\beta} - RV_{H\gamma}$, respectively. The non-zero mean RV differences between Hα, Hβ, and Hγ lines are largely due to the existence of a wavelength-dependent residual after the wavelength calibration. We therefore convert $RV_{H\alpha}$ and $RV_{H\beta}$ to the scale of $RV_{H\gamma}$ by subtracting 14.59 and 5.83 km s^{-1} from the measured values, respectively.

The final value of RV of a target is calculated by combining results from all three Balmer lines, namely

$$RV = \frac{RV_{H\alpha}/\sigma_\alpha^2 + RV_{H\beta}/\sigma_\beta^2 + RV_{H\gamma}/\sigma_\gamma^2}{1/\sigma_\alpha^2 + 1/\sigma_\beta^2 + 1/\sigma_\gamma^2}, \quad (5)$$

$$\sigma_{RV} = \sqrt{\frac{1}{1/\sigma_\alpha^2 + 1/\sigma_\beta^2 + 1/\sigma_\gamma^2}}. \quad (6)$$

We note that the systemic radial velocities of Type c RRLs can also be derived, using the template radial-velocity curves for Types ab RRLs, but only the systemic radial velocities of Type ab RRLs are recommended.

4.2. Validation with Reference Stars

In order to check the uncertainties (both random and systemic) of our measurements, we collect RRLs from the literature with reliable radial-velocity measurements from high-resolution spectroscopy; GC members are also included (Dambis 2009; Harris 2010; Kinman et al. 2012; Britavskiy et al. 2018). In total, 108 common stars are found and their relevant information is listed in Table 5. (The information of 29 GC members has been listed in Table 2.) Figure 7 shows the comparisons. The standard derivations of the differences are 20.6, 14.6, 9.7, and 4.5 km s^{-1} for $n = 1$, 2, 3, and $\geqslant$4, respectively. The median values of the differences are all around 2 km s^{-1}, indicating no significant systemics of our final derived radial velocities. We do not correct such a small offset since it is much smaller than the standard deviations. The results show that once the number of radial-velocity measurements available to fit the radial-velocity curve is great than 2, the standard deviation of the systemic velocity derived is likely to be less than 10 km s^{-1}. The expected uncertainty drops to only 4.5 km s^{-1} for $n \geqslant 4$. This indicates our velocity measurements are quite robust.

Although the pulsating nature of RRLs makes the determinations of their systemic radial velocities more difficult than that for other nonpulsating normal stars (e.g., Layden 1994; Vivas et al. 2005; Prior et al. 2009), this work shows that one can still use the large numbers of low-resolution spectroscopic observations to derive systemic radial velocities with precisions between 5 and 21 km s^{-1}. This precision is adequate for studying the Galactic halo properties considering that the line-of-sight velocity dispersion of halo stars is around 100 km s^{-1} (e.g., Huang et al. 2016).

4.3. Discussion

Sesar (2012) shows that the amplitude of the template radial-velocity curve of RRLs is a function of the amplitude of V-band light curve (A_V). However, because only part of the RRLs in our catalog have A_V available, we fixed the amplitude of the template radial-velocity curve in the fitting to derive the systemic radial velocity (see Section 4.1). To evaluate the effects of our constant radial-velocity curve amplitude choice for deriving the systemic radial velocities of RRLs, we redetermine the systemic radial velocities of >2000 RRLs with A_V known. At this time, we repeat the fitting described in Section 4.1 using the values of A_{rv} determined by A_V from the functions provided by Sesar (2012) and obtain their new systemic radial velocities.

By comparing the new results with our adopted ones, the median velocity difference is found around 2 km s^{-1} and the standard deviation of the velocity difference is only about 4 km s^{-1}. According to the above test, our constant radial-velocity curve amplitude choices show minor effects upon deriving the systemic radial velocities of RRLs.

The new values of systemic radial velocity determined in this section are also in the final catalog for reference.

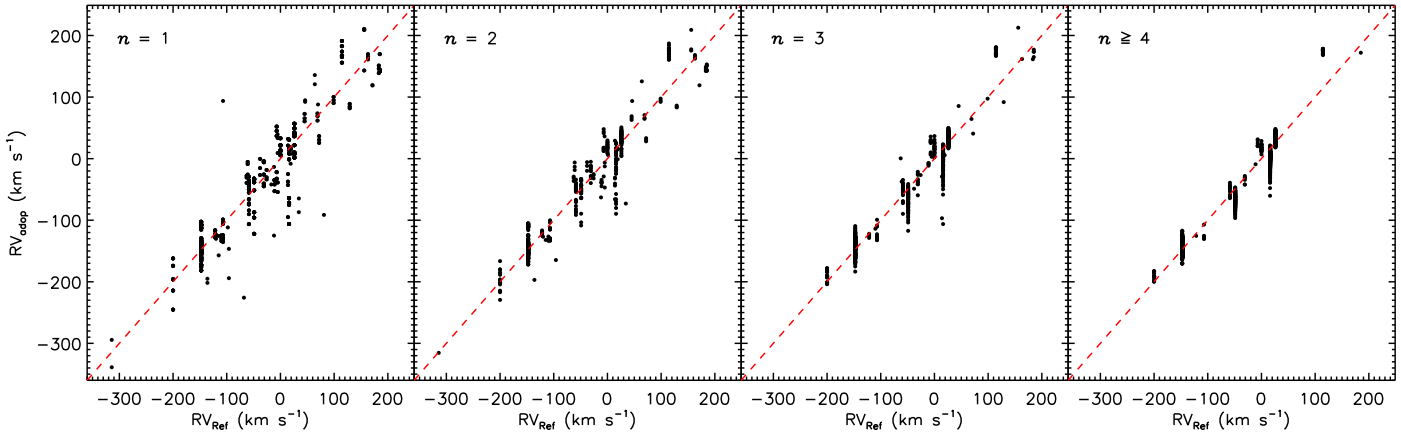

Figure 7. Comparisons of systemic radial velocities derived in the current work and those from literature. The standard deviations are 20.6, 14.6, 9.7 and 4.5 km s^{-1} for $n = 1$, 2, 3, and $\geqslant 4$, respectively.

Table 5
Radial Velocities of Reference Stars Selected from the Literature

Star	R.A. (degree)	Decl. (degree)	RV_{Ref} (km s^{-1})	Error of RV_{Ref} (km s^{-1})	Reference …	Star	R.A. (degree)	Decl. (degree)	RV_{Ref} (km s^{-1})	Error of RV_{Ref} (km s^{-1})	Reference …
DR Vir	16.295	34.218	−110.000	4.000	B18	XX And	19.364	38.951	0.000	1.000	D09
CI And	28.785	43.767	24.000	5.000	D09	BK Eri	42.483	−1.420	141.000	10.000	D09
SS Tau	54.174	5.361	−11.000	10.000	D09	TU Per	47.270	53.193	−314.200	0.500	D09
AR Per	64.322	47.400	5.000	1.000	D09	SZ Vir	118.431	19.273	346.000	6.000	B18
RR Gem	110.390	30.883	64.000	1.000	D09	YY Lyn	116.375	37.383	−93.100	15.000	K12
ZZ Lyn	117.591	37.700	147.000	15.000	D09	VY Lyn	113.108	38.835	114.500	15.000	K12
AC Lyn	118.675	38.906	−25.800	15.000	K12	VX Lyn	112.966	39.130	1.000	15.000	D09
WX Lyn	113.910	39.257	26.000	15.000	D09	TZ Aur	107.896	40.777	45.000	2.000	D09
VZ Lyn	113.170	41.627	−182.100	15.000	K12	TW Lyn	116.276	43.112	−39.000	1.000	D09
DD Hya	123.132	2.835	156.000	1.000	D09	AN Cnc	134.543	15.805	16.000	14.000	D09
AF Lyn	128.989	41.020	−121.700	15.000	K12	P 54-13	120.484	41.022	69.000	10.000	K12
T Sex	148.369	2.057	29.000	1.000	D09	BS 16927	146.151	41.143	70.000	10.000	K12
TT Lyn	135.784	44.586	−65.000	2.000	D09	SW Leo	163.981	−2.982	46.000	11.000	D09
BK UMa	162.579	42.569	171.400	5.000	K12	TV Leo	167.841	−5.892	−96.000	5.000	D09
SS Leo	173.477	−0.033	163.000	2.000	D09	SZ Leo	165.404	8.166	185.000	4.000	D09
AE Leo	171.551	17.661	−53.000	10.000	D09	BN UMa	169.095	41.234	19.000	10.000	K12
BQ Vir	189.114	−2.426	129.000	9.000	D09	UV Vir	185.320	0.368	99.000	11.000	D09
FU Vir	189.610	13.016	−90.000	8.000	D09	S Com	188.190	27.029	−55.000	1.000	D09
DV Com	190.977	28.021	−136.000	10.000	D09	EO Com	194.342	28.889	72.000	10.000	D09
EM Com	192.910	30.518	−127.000	10.000	D09	CD Com	183.142	30.801	−203.000	10.000	D09
TU Com	183.446	30.985	−98.000	10.000	D09	CK UMa	180.402	31.903	16.000	10.000	K12
CK Com	183.711	33.102	−88.000	10.000	D09	DC CVn	191.818	35.202	−200.000	10.000	D09
SW Vir	190.229	37.085	14.000	6.000	B18	UZ Vir	187.615	40.509	−49.000	6.000	B18
Z CVn	192.439	43.774	14.000	10.000	D09	WW Vir	202.099	−5.286	129.000	10.000	D09
BC Vir	200.588	5.886	4.000	13.000	D09	BB Vir	207.920	6.431	−38.000	13.000	D09
AV Vir	200.048	9.188	153.000	1.000	D09	UY Boo	209.693	12.952	145.000	2.000	D09
ST Com	199.464	20.781	−68.000	10.000	D09	RY Com	196.283	23.278	−31.000	8.000	D09
ST CVn	209.392	29.858	−129.000	1.000	D09	EW Com	198.257	31.023	19.000	10.000	D09
RZ CVn	206.263	32.655	−12.000	1.000	D09	SS CVn	207.066	39.901	−40.000	3.000	D09
RV Vir	203.325	53.988	−175.000	6.000	B18	SX UMa	201.556	56.257	−154.000	1.000	D09
AE Vir	216.872	3.778	208.000	10.000	D09	RS Boo	218.389	31.755	−7.000	1.000	D09
TW Vir	221.275	41.029	−89.000	2.000	B18	AN Ser	238.379	12.961	81.000	1.000	C17
BH Ser	228.754	19.443	−113.000	11.000	D09	AW Ser	241.620	15.368	−126.000	15.000	D09
RW Dra	248.882	57.840	−112.000	1.000	D09	V0816 Oph	265.658	4.958	−28.000	10.000	D09
V0784 Oph	263.855	7.756	−167.000	10.000	D09	DL Her	260.094	14.511	−61.000	14.000	D09
TW Her	268.630	30.410	−5.000	1.000	D09	VZ Her	258.267	35.979	−115.000	1.000	D09
KX Lyr	278.314	40.173	−36.200	0.500	D09	SX Aqr	324.035	3.231	−165.000	3.000	D09
AO Peg	321.765	18.599	264.000	4.000	D09	VV Peg	333.266	18.451	34.200	0.000	D09
DZ Peg	350.029	16.069	−289.500	2.400	D09	VZ Peg	355.568	24.916	−264.000	1.000	D09
BK And	353.775	41.103	−17.000	7.000	D09	…	…	…	…	…	…

Note. The references are: (B18) Britavskiy et al. (2018), (D09) Dambis (2009), (K12) Kinman et al. (2012), (C17) Chadid et al. (2017).

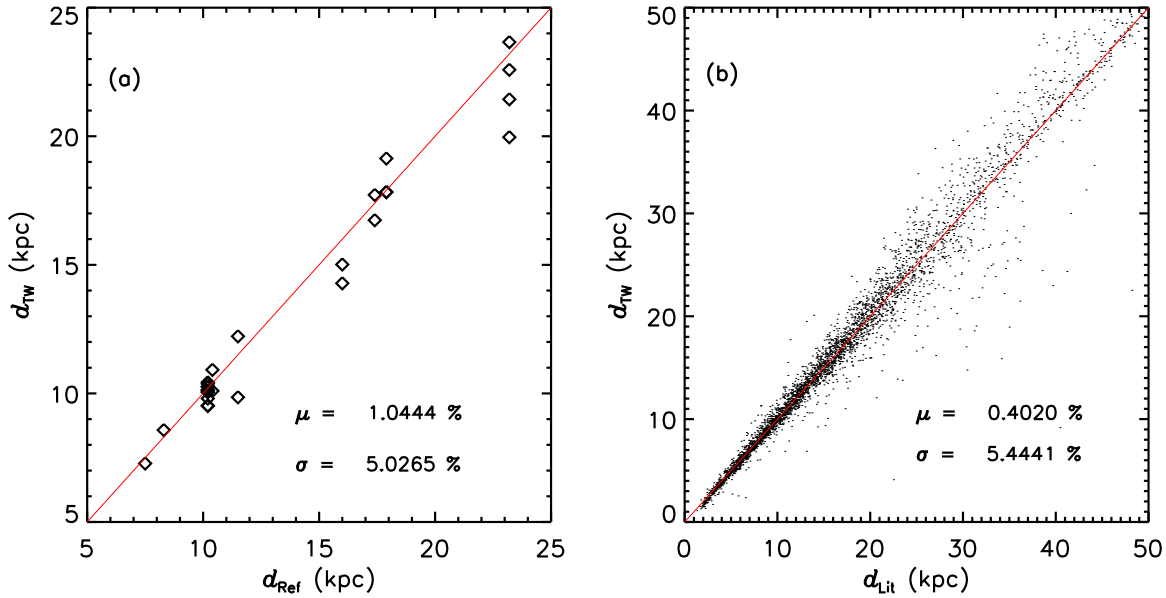

Figure 8. Panel (a) compares distances derived in this work (d_{TW}) with reference values from the star cluster catalog (d_{Ref}). Panel (b) is comparison but with reference values collected from other sources in the literature (d_{Lit}).

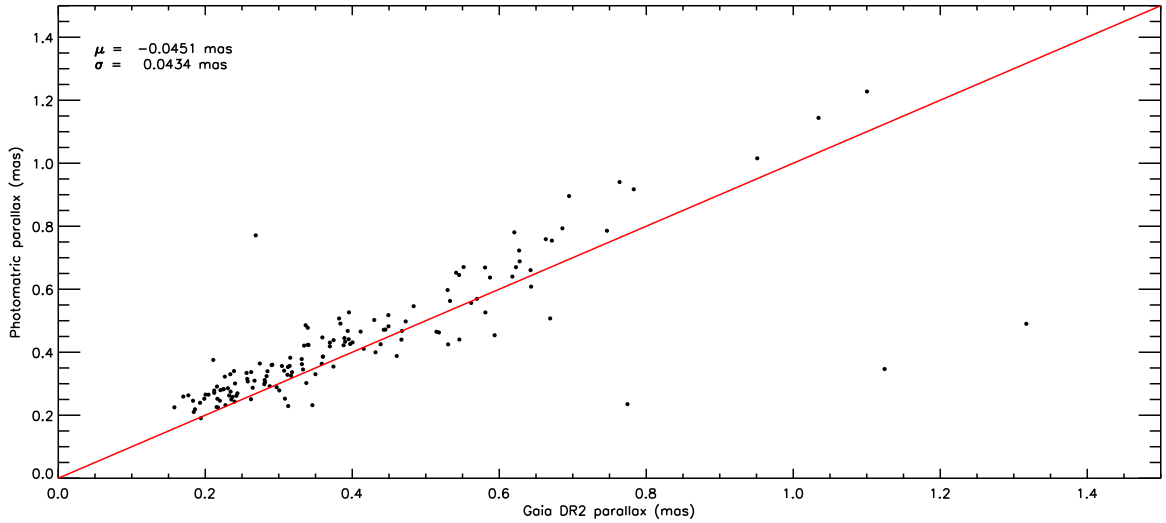

Figure 9. Comparison of parallaxes converted from distances derived in the current work and those measured by the *Gaia* DR2 for RRab stars.

5. Distances

5.1. Measurement Method

Generally, RRLs are divided into three types: Type ab RRLs (RRab) pulsate in the fundamental mode, Type c RRLs (RRc) pulsate in the first-overtone mode, and Type d RRLs (RRd) pulsate in both modes simultaneously. In our sample, the number of RRd is small, so we do not discuss them separately. Being standard candles, RRLs obey the well-defined relations between absolute visual magnitude and metallicity:

$$M_V = a\ [\mathrm{Fe/H}] + b, \tag{7}$$

and the near- or mid-infrared period-absolute magnitude-metallicity (*PMZ*),

$$M_{K_s/W_1} = c\ \log(\mathrm{P}) + d\ [\mathrm{Fe/H}] + e. \tag{8}$$

Coefficients a, b, c, d, e are different for Type ab and Type c RRLs. In this paper, for RRab, coefficients a, b, c, d, e are taken from Muraveva et al. (2018), derived using the latest data of *Gaia* DR2 (please refer to their Table 4 for more detail). For RRc, coefficients a, b given by Ferro et al. (2017) are used. We adopt the mid-infrared period-absolute magnitude relation provided by Klein et al. (2014):

$$M_{W1} = -1.64\log(\mathrm{P}/0.32) - 0.231. \tag{9}$$

Compared to the visual M_V–[Fe/H] relation, near- or mid-infrared *PMZ* relations are less affected by interstellar extinction. In the following calculations, we prefer distances derived from the near/mid-infrared *PMZ* relations as the final ones.

We cross match our sample with the 2MASS and *Wide-field Infrared Survey Explorer* (*WISE*) catalogs to obtain apparent magnitudes in the K_s and $W1$ bands for our sample stars. For sources selected from the Catalina survey, Catalina V-band magnitudes are converted to Johnson V-band magnitudes using the transformation equation of Graham et al. (2015), assuming an intrinsic $(B-V)_0$ color of 0.2 for RRLs. We then use the

Table 6
Columns of the RRLs Catalog

	Column	Unit	Description
1	ID	...	A unique object id for the cataloged RRLs
2	R.A.	degree	R.A. at J2000 from the photometric surveys
3	Decl.	degree	decl. at J2000 from the photometric surveys
4	GL	degree	Galactic longitude
5	GB	degree	Galactic latitude
6	VMAG	mag	*V*-band magnitude
7	ERR-VMAG	mag	Error in *V*-band magnitude
8	PER	day	Period
9	PFROM	...	Reference for period
10	EPOCH	day	Date of maximum light from the photometric surveys
11	EPOCH-FLG	...	Which type of EPOCH (MJD, JD, HJD)
12	VARTYPE	...	Type
13	S/N	...	Spectral S/N at 4650 Å
14	FEH-ADOP	dex	Metallicity derived in the current work
15	ERR-FEH-ADOP	dex	Error of FEH-ADOP
16	FEH-REF	dex	Metallicity from the literature if available
17	ERR-FEH-REF	dex	Error of FEH-REF
18	RV-ADOP[a]	km s^{-1}	Systemic radial velocity derived in the current work
19	ERR-RV-ADOP	km s^{-1}	Error of RV-ADOP
20	RV-REF1	km s^{-1}	Systemic radial velocity determined in Section 4.3
21	ERR-RV-REF1	km s^{-1}	Error of RV-REF1
22	RV-REF2	km s^{-1}	Systemic radial velocity from the literature if available
23	ERR-RV-REF2	km s^{-1}	Error of RV-REF2
24	DIST-ADOP	kpc	Distance derived in the current work
25	ERR-DIST-ADOP	kpc	Error of DIST-ADOP
26	DIST-REF	kpc	Distance from the literature if available
27	ERR-DIST-ADOP	kpc	Error of DIST-ADOP
28	PMRA	mas yr^{-1}	Proper motion in $\alpha \cos\delta$ from *Gaia* DR2
29	PMDEC	mas yr^{-1}	Proper motion in δ from *Gaia* DR2
30	ERR-PMRA	mas yr^{-1}	Error of the proper motion in $\alpha\cos\delta$ from *Gaia* DR2
31	ERR-PMDEC	mas yr^{-1}	Error of the proper motion in δ from *Gaia* Dr2
32	NUMBER	...	Number of individual spectra available

Note.
[a] The radial velocities for type c RRLs are not recommended for use.

above relations to obtain the absolute magnitudes and further derive the distances after the interstellar extinction corrections.

Actually, the *WISE* magnitudes could have been taken as mean magnitudes since they are the mean values typically of $\geqslant$10 single-epoch observations obtained by the *WISE* survey (Wright et al. 2010). We therefore derive the distances of RRLs from the *W*1 band if uncertainties smaller than 0.1 mag. For only 13 stars without good *W*1-band photometry but with K_s-band photometry, we derive their distances from the K_s band. If both K_s- and *W*1-band photometric uncertainties do not meet our requirements, we use the visual M_V–[Fe/H] relation to obtain the distance.

In total we obtain distances for 4919 RRLs with the above procedures (4061 from the *W*1 band, 13 from the K_s band, and 845 from the *V* band).

5.2. Validation of Distances

5.2.1. Comparison with Reference Stars

In order to check the reliability of our calculations, we first compare the distances obtained above with those in the literature for the reference sample, for which the reference distances were obtained from the star cluster catalog. As shown in Figure 8, the average relative difference ($\frac{\Delta d}{d}$) is about 1%, with a dispersion of about 5%. We also collect information for distances from other sources in the literature (Vivas & Zinn 2006; Miceli et al. 2008; Watkins et al. 2009; Süveges et al. 2012; Drake et al. 2013a, 2013b; Sesar et al. 2013). The comparison is also shown in Figure 8. We find that they all agree very well with each other.

5.2.2. Comparison with Gaia Parallaxes

We also compare our distances measurements with the *Gaia* parallaxes. We first convert our distances estimates of uncertainties less than 10%, derived from near- or mid-infrared or visual magnitudes, into photometric parallaxes, then compare them with those from the *Gaia* DR2. Figure 9 shows the comparison for RRab stars. The mean deviation is −0.04 mas, consistent with the zero-point offset reported by the *Gaia* collaboration (Gaia Collaboration et al. 2018). As seen in Figure 9, four outliers significantly deviate from one-to-one line. We have checked the distances derived here against those from the literature and find they are all consistent. The reasons for those outliers are still unclear and one possible

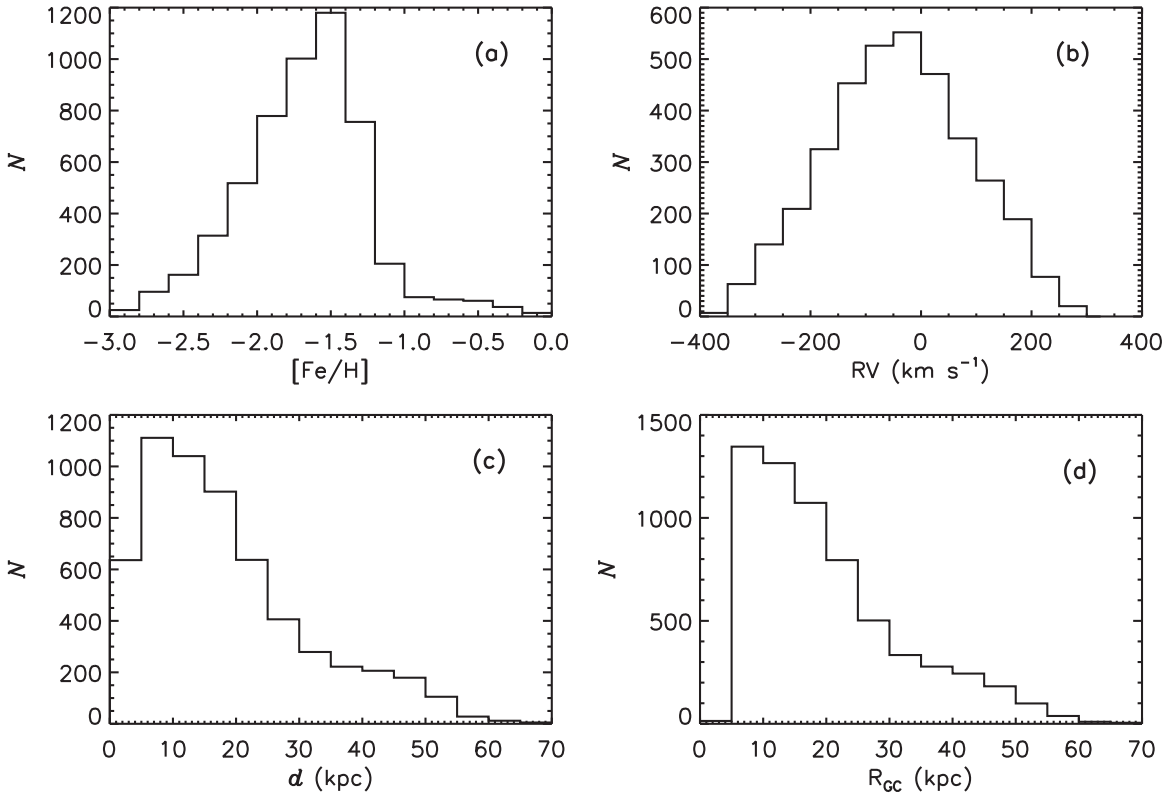

Figure 10. Panel shows the distributions of (a) metallicities, (b) systemic radial velocities, (c) distance, and (d) distances to the center of the Galaxy derived in the current work for stars in the final main catalog.

explanation is that their parallax solutions are somehow wrong. Similar results are found for RRc stars.

6. The Final Catalog

By combing the SDSS and LAMOST spectroscopic data with the photometric data of objects in the literature, we have compiled a catalog of RRLs containing 6268 unique RRLs. For objects with individual single-exposure S/Ns greater than 10 and not affected by shock waves, we measure the metallicities by a least χ^2 fitting technique. The weighted mean metallicities of the individual spectra are adopted as the final values. In total, metallicities for 5290 RRLs are obtained in this way. We then fit the templates of systemic velocity of RRLs provided by Sesar (2012) to the observed ones and derive the systemic radial velocity for 3642 RRLs. Finally, we use the *PMZ* or M_V–[Fe/H] relations to calculate the distances of our sample stars and obtain distance estimates for 4919 RRLs. All the information derived is compiled into an online catalog containing 6268 RRLs (Table 6). Table 6 lists the columns contained in the main catalog. Figure 10 shows the distributions of metallicities, systemic radial velocities, distances, and Galactocentric distances of stars in the final main catalog.

In the near future, we plan to enlarge our sample by including data from additional spectroscopic surveys, e.g., the GALAH survey (De Silva et al. 2015), as well as additional photometrically identified RRLs from the recent time-domain surveys, e.g., Pan-STARRS1 (Chambers et al. 2016; Sesar et al. 2017) and the *Gaia* DR2 (Clementini et al. 2019). We expect to have precise measurements of metallicities, systemic radial velocities and distances of RRLs for the whole sky. The data shall be very helpful for the study of the formation and evolution of the Galactic halo.

7. Conclusion

We present a catalog of 5290 RRLs with metallicity estimates. Nearly 70% of them also have systemic radial-velocity measurements. We use the single-exposure spectra rather than the combined spectra for metallicity and velocity estimation. We develop a criterion based on the measured EW of Ca II K line, EW(Ca II K), to diagnose whether a spectrum is affected by shock waves or not. Those affected are excluded, from the metallicity and velocity estimation.

We measure the systemic radial velocities using the empirical template radial-velocity curves of RRLs provided by Sesar (2012) and obtain results for 3642 RRLs in total. The typical error is about 5 $\sim$ 21 km s^{-1}, dependent on the number of radial-velocity measurements available at different phases.

Finally, with the well calibrated near-infrared $PM_{K_s}Z$ or $PM_{W1}Z$, and M_V–[Fe/H] relations, precise distances are derived for 4919 RRLs.

The results provide vital information to study many issues related to the Galactic halo.

We thank the anonymous referee for his/her helpful suggestions and comments. This work is supported by the National Science Foundation of China under grant No. U1731108 and 11903027 and Natural Science Foundation of CTGU under grant No. KJ2014B078. This work is also supported by the National Key R&D Program of China No. 2019YFA0405500. Y. H., B.Q.C., and X.W.L. acknowledge the National Natural Science Foundation of China U1531244, 11833006, and 11811530289. H.W.Z. acknowledge the National Natural Science Foundation of China 11973001. The Guoshoujing Telescope (the Large Sky Area Multi-Object Fiber Spectroscopic Telescope LAMOST) is a National Major

Scientific Project built by the Chinese Academy of Sciences. Funding for the project has been provided by the National Development and Reform Commission. LAMOST is operated and managed by the National Astronomical Observatories, Chinese Academy of Sciences.

This work has made use of data from the European Space Agency (ESA) mission *Gaia* (https://www.cosmos.esa.int/gaia), processed by the *Gaia* Data Processing and Analysis Consortium (DPAC, https://www.cosmos.esa.int/web/gaia/dpac/consortium). This work also has made use of data products from the SDSS, 2MASS, and *WISE*.

ORCID iDs

M.-S. Xiang https://orcid.org/0000-0002-5818-8769

References

Alam, S., Albareti, F. D., Allende, P., et al. 2015, ApJS, 219, 12
Alcock, C., Alves, D. R., Becker, A., et al. 2003, ApJ, 598, 597
Armosky, B. J., Sneden, C., Langer, G. E., & Kraft, R. P. 1994, AJ, 108, 1364
Belokurov, V., Erkal, D., Evans, N. W., et al. 2018, MNRAS, 478, 611
Britavskiy, N., Pancino, E., Tsymbal, V., Romano, D., & Fossati, L. 2018, MNRAS, 474, 3344
Brown, W. R., Geller, M. J., Kenyon, S. J., et al. 2010, AJ, 139, 59
Butler, D. 1975, ApJ, 200, 68B
Cacciari, C., Corwin, T. M., & Carney, B. W. 2005, AJ, 129, 267
Carlin, J. L., Majewski, S. R., Casetti-Dinescu, D. I., et al. 2012, ApJ, 744, 25C
Carretta, E., Bragaglia, A., Gratton, R., et al. 2009, A&A, 508, 695C
Casetti-Dinescu, D. I., Giaard, T. M., Majewski, S. R., et al. 2009, ApJ, 701, 29
Castelli, F., & Kurucz, R. L. 2003, in IAU Symp. 210, Modelling of Stellar Atmospheres, ed. N. Piskunov, W. W. Weiss, & D. F. Gray (Cambridge: Cambridge Univ. Press), A20
Chaboyer, B., Green, E. M., & Liebert, J. 1999, AJ, 117, 1360
Chadid, M., Sneden, C., & Preston, G. W. 2017, ApJ, 835, 187C
Chambers, K. C., Magnier, E. A., Metcalfe, N., et al. 2016, arXiv:1612.05560
Clement, C. M. 2017, yCat, 5150
Clementini, G., Carretta, E., Gratton, R., et al. 1995, AJ, 110, 2319
Clementini, G., Ripepi, V., Molinaro, R., et al. 2019, A&A, 622A, 60c
Cohen, J. G., & Meléndez, J. 2005, AJ, 129, 303
Cui, X. Q., Zhao, Y. H., Chu, Y. Q., et al. 2012, RAA, 12, 1197
Dambis, A. K. 2009, MNRAS, 396, 553
Das, P., Williams, A., & Binney, J. 2016, MNRAS, 463, 3169
De Silva, G. M., Freeman, K. C., Bland-Hawthorn, J., et al. 2015, MNRAS, 449, 2604
Deason, A. J., Belekurov, V., Evans, N. W., et al. 2011, MNRAS, 416, 2903
Deason, A. J., Belekurov, V., Koposov, S. E., et al. 2014, ApJ, 787, 30
Deng, L. C., Newberg, H. J., Liu, C., et al. 2012, RAA, 12, 735
Drake, A. J., Catelan, M., Djorgovski, S. G., et al. 2013a, ApJ, 765, 154
Drake, A. J., Catelan, M., Djorgovski, S. G., et al. 2013b, ApJ, 763, 32D
Drake, A. J., Graham, M. J., Djorgovski, S. G., et al. 2014, ApJS, 213, 9D
Fabrizio, M., Bono, G., Braga, V. F., et al. 2019, ApJ, 883, 31
Ferro, A. A., Bramich, D. M., & Giridhar, S. 2017, RMxAA, 53, 121
Fokin, A. B. 1992, MNRAS, 256, 26F
For, B. Q., Sneden, C., & Preston, G. W. 2011, ApJS, 197, 29
Freeman, K. C., & Rodgers, A. W. 1975, ApJ, 201L, 71F
Fusi Pecci, F., Buonanno, R., Cacciari, C., et al. 1996, AJ, 112, 1461
Gaia Collaboration, Brown, A. G. A., Vallenari, A., et al. 2016, A&A, 595, A2
Gaia Collaboration, Helmi, A., van Leeuwen, F., et al. 2018, A&A, 616, A12
Gillet, D., & Fokin, A. B. 2004, A&A, 565, 73
Govea, J., Gomez, T., Preston, G. W., et al. 2014, ApJ, 782, 59
Graham, M. J., Diorgovski, S. G., Stern, D., et al. 2015, Natur, 518, 74
Gray, R. O. 1999, SPECTRUM: A stellar spectral synthesis program, ascl:9910.002
Harris, W. E. 2010, arXiv:1012.3224
Hoffman, D. I., Harrison, T. E., & McNamara, B. J. 2009, AJ, 138, 466
Huang, Y., Liu, X. W., Yuan, H. B., et al. 2016, MNRAS, 463, 2623
Keller, S. C., Murphy, S., Prior, S., et al. 2008, ApJ, 678, 851
Kinemuchi, K., Smith, H. A., Woniak, P. R., et al. 2006, AJ, 132, 1202K
Kinman, T. D., Cacciari, C., Bragaglia, A., et al. 2012, MNRAS, 422, 2116
Klein, C. R., Richards, J. W., Butler, N. R., & Bloom, J. S. 2014, MNRAS, 440, 96
Kraft, R. P., Sneden, C., Langer, G. E., Prosser, & Charles, F. 1992, AJ, 104, 645
Layden, A. C. 1994, AJ, 108, 1016L
Liu, X. W., Yuan, H.-B., Huo, Z.-Y., et al. 2014, in IAU Symp. 298, Setting the Scene for Gaia and LAMOST, ed. S. Feltzing et al. (Cambridge: Cambridge Univ. Press), 310
Majewski, S. R., Schiavon, R. P., Frinchaboy, P. M., et al. 2017, AJ, 154, 94
Mateu, C., Vivas, A. K., Downes, J. J., et al. 2012, MNRAS, 427, 3374
Miceli, A., Rest, A., Stubbs, C. W., et al. 2008, ApJ, 678, 865
Muraveva, T., Delgado, H. E., Clementini, G., et al. 2018, MNRAS, 481, 1195
Nemec, J. M., Cohen, J. G., Ripepi, V., et al. 2013, ApJ, 773, 181
Pancino, E., Britavskiy, N., Romano, D., et al. 2015, MNRAS, 447, 2404
Pila-Diez, B., de Jong, J. T. A., Kuijken, K., et al. 2015, A&A, 579, 38
Pojmanski, G. 2002, AcA, 52, 397
Preston, G. W. 1959, ApJ, 130, 507
Prior, S. L., Da Costa, G. S., Keller, S. C., et al. 2009, ApJ, 691, 306
Ren, J. J., Liu, X. W., Xiang, M. S., et al. 2016, RAA, 16, 45
Samus, N. N., Kazarovets, E. V., Kireeva, N. N., et al. 2010, OAP, 23, 102
Samus, N. N., Kazarovets, E. V., Pastukhova, E. N., et al. 2009, PASP, 121, 1378
Sandage, A. 1993, AJ, 106, 703
Sandstrom, K., Pilachowski, C. A., & Saha, A. 2001, AJ, 122, 3212
Sesar, B. 2012, AJ, 144, 114
Sesar, B., Hernitschek, N., Mitrović, S., et al. 2017, AJ, 153, 204s
Sesar, B., Ivezić, Ž., Grammer, S. H., et al. 2010, ApJ, 708, 717
Sesar, B., Ivezić, Ž., Stuart, J. S., et al. 2013, AJ, 146, 21
Sesar, B., Jurić, M., & Ivezić, Ž. 2011, ApJ, 731, 4s
Smith, H. A. 2004, RR Lyrae Stars (Cambridge: Cambridge Univ. Press)
Steinmetz, M., Zwitter, T., Siebert, A., et al. 2006, AJ, 132, 1645
Süveges, M., Sesar, B., Váradi, M., et al. 2012, MNRAS, 424, 2528
Vivas, A. K., & Zinn, R. 2006, AJ, 132, 714V
Vivas, A. K., Zinn, R., Abad, C., Andrews, P., et al. 2004, AJ, 127, 1158V
Vivas, A. K., Zinn, R., Andrews, P., et al. 2001, ApJ, 554L, 33V
Vivas, A. K., Zinn, R., & Gallart, C. 2005, AJ, 129, 189
Wang, S. G., Su, D. Q., Chu, Y. Q., Cui, X. Q., & Wang, Y. N. 1996, ApOpt, 35, 5155
Watkins, L. L., Evans, N. W., Belokurov, V., et al. 2009, MNRAS, 398, 1757
Wolf, C., Onken, C. A., Luvaul, L. C., et al. 2018, PASA, 35, e010
Wright, E. L., Eisenhardt, P. R. M., Mainzer, A. K., et al. 2010, AJ, 140, 1868
Xiang, M. S., Liu, X. W., Yuan, H. B., et al. 2015, MNRAS, 448, 822
Xiang, M. S., Liu, X. W., Yuan, H. B., et al. 2017, MNRAS, 467, 1890
Xu, Y., Liu, C., Xue, X. X., et al. 2018, MNRAS, 473, 1244
Xue, X. X., Rix, H. W., Ma, Z., et al. 2015, ApJ, 809, 144
Xue, X. X., Rix, H. W., Zhao, G., et al. 2008, ApJ, 684, 1143
Yanny, B., Rockosi, C., Newberg, H. J., et al. 2009, AJ, 137, 4377
Yuan, H. B., Liu, X. W., Huo, Z. Y., et al. 2015, MNRAS, 448, 855
Zhao, G., Zhao, Y. H., Chu, Y. Q., et al. 2012, RAA, 12, 723
Zinn, R., Horowitz, B., Vivas, A. K., et al. 2014, ApJ, 781, 22Z
Zinn, R., & West, M. J. 1984, ApJS, 55, 45